Naval Research Laboratory

Washington, DC 20375-5320

NRL/MR/5341--20-10,083

Sparse Aperture Multistatic Radar Imaging Techniques: FY19 Summary Report

Matthew Burfeindt

Hatim Alqadah

Surveillance Technology Branch
Radar Division

September 14, 2020

REPORT DOCUMENTATION PAGE

Form Approved
OMB No. 0704-0188

1. REPORT DATE *(DD-MM-YYYY)*	**2. REPORT TYPE**	**3. DATES COVERED** *(From - To)*
14-09-2020	NRL Memorandum Report	1 Oct 2018 to 1 Oct 2019

4. TITLE AND SUBTITLE

Sparse Aperture Multistatic Radar Imaging Techniques: FY19 Summary Report

5a. CONTRACT NUMBER

5b. GRANT NUMBER

5c. PROGRAM ELEMENT NUMBER

6. AUTHOR(S)

Matthew Burfeindt and Hatim Alqadah

5d. PROJECT NUMBER

5e. TASK NUMBER

5f. WORK UNIT NUMBER
1L40

7. PERFORMING ORGANIZATION NAME(S) AND ADDRESS(ES)

Naval Research Laboratory
4555 Overlook Avenue, SW
Washington, DC 20375-5320

8. PERFORMING ORGANIZATION REPORT NUMBER

NRL/MR/5341--20-10,083

9. SPONSORING / MONITORING AGENCY NAME(S) AND ADDRESS(ES)

Naval Research Laboratory
4555 Overlook Avenue, SW
Washington, DC 20375-5320

10. SPONSOR / MONITOR'S ACRONYM(S)

11. SPONSOR / MONITOR'S REPORT NUMBER(S)

12. DISTRIBUTION / AVAILABILITY STATEMENT

DISTRIBUTION STATEMENT A: Approved for public release; distribution is unlimited.

13. SUPPLEMENTARY NOTES

14. ABSTRACT

We report the results of two studies on multistatic radar imaging from a sparse receiver set using new formulations of the qualitative inverse scattering technique known as the Linear Sampling Method (LSM). First, we introduce and evaluate an LSM formulation for improving sparse-receiver imaging by incorporating a priori phase delay information into the imaging technique. Secondly, we introduce and evaluate a technique for monostatic LSM imaging that leverages multifrequency information. For both studies, we report promising imaging results from simulated data acquisitions.

15. SUBJECT TERMS

Radar
Inverse scattering
Multistatic
Sparsity

16. SECURITY CLASSIFICATION OF:			**17. LIMITATION OF ABSTRACT**	**18. NUMBER OF PAGES**	**19a. NAME OF RESPONSIBLE PERSON**
a. REPORT	**b. ABSTRACT**	**c. THIS PAGE**			Matthew Burfeindt
Unclassified Unlimited	Unclassified Unlimited	Unclassified Unlimited	Unclassified Unlimited	16	**19b. TELEPHONE NUMBER** *(include area code)* (608) 417-9833

Standard Form 298 (Rev. 8-98)
Prescribed by ANSI Std. Z39.18

This page intentionally left blank.

SPARSE APERTURE MULTISTATIC RADAR IMAGING TECHNIQUES: FY19 SUMMARY REPORT

Matthew J. Burfeindt and Hatim F. Alqadah
NRL Radar Division, Surveillance Technology Branch

ABSTRACT

We report the results of two studies on multistatic radar imaging from a sparse receiver set using new formulations of the qualitative inverse scattering technique known as the Linear Sampling Method (LSM). First, we introduce and evaluate an LSM formulation for improving sparse-receiver imaging by incorporating a priori phase delay information into the imaging technique. Secondly, we introduce and evaluate a technique for monostatic LSM imaging that leverages multifrequency information. For both studies, we report promising imaging results from simulated data acquisitions.

1. INTRODUCTION

Qualitative inverse scattering refers to a class of imaging technique in which the shape, but not the electrical properties, of a target is reconstructed based on scattered electric fields. The Linear Sampling Method (LSM) [1] is a technique in this class that has several advantageous properties. It involves solving a linear system, and as such is relatively straightforward and computationally inexpensive to implement. It is also formulated without using any linear scattering assumptions, and is thus robust to imaging artifacts from multi-bounce phenomena that sometimes corrupts synthetic aperture radar (SAR) imagery.

However, the LSM relies on spatially dense multistatic, multiview data in order to form faithful imagery. This type of data is often not available in practical imaging scenarios due to limited resources or data acquisition time. New formulations of the LSM that are effective in sparse-aperture data acquisition scenarios are thus of interest.

In this memo report, we present the results of investigations into this problem that took place in FY19 as part of a project funded by the NRL 6.1 Base Program under work unit 1L40. The report is broken into two remaining sections. In Sec. 2, we improve imaging performance in sparse-aperture scenarios by incorporating *a priori* propagation information into the LSM inversion. In Sec. 3, we introduce a technique for monostatic LSM imaging based on a multistatic data completion strategy.

2. SPARSE APERTURE QUALITATIVE INVERSE SCATTERING USING A PHASE-DELAY-BASED FREQUENCY VARIATION CONSTRAINT

This section is adapted from a paper published in the 2019 Proceedings of the IEEE Research and Applications of Photonics in Defense Conference [2].

2.1 Background

Application of the standard single-frequency LSM to data sets that are limited in either transmitter or receiver locations will often result in significant imaging artifacts. Such artifacts can sometimes be mitigated using multifrequency data. In most studies, this strategy is implemented by finding the LSM solution for each frequency independently and then summing the solutions non-coherently to form the final

Manuscript approved September 11, 2020.

image. Assuming the LSM solutions for locations inside the target are more consistent across frequency as compared to solutions for artifact locations, the non-coherent sum can be expected to enhance the image contrast between pixels inside and outside the target support. However, the quality of the final image is still dependent on the degree of aberrance in the single-frequency solutions. Furthermore, previous studies suggest that this approach to multifrequency LSM is ineffective in the challenging case where only a few observation directions are available, even if the transmit aperture is densely sampled (and vice versa, via the electromagnetic principle of reciprocity) [1] [3] [4]. Alternative strategies for multifrequency LSM imaging are thus warranted.

A well-known approach for improving the inversion behavior for ill-posed inverse problems is to incorporate constraints based on *a priori* assumptions about the solution. To our knowledge there has not been much, if any, work that attempts to explicitly leverage assumptions on the phase of the LSM solution.

The phase of the scattered field, and thus the phase of the LSM solution, is related to the electrical distance traversed by the incident electric field. In this paper, we will use this concept to link the LSM solutions across frequency according to the expected phase delay between the antennas and each imaging scene pixel. Previous work has demonstrated imaging improvements in sparse-aperture scenarios by penalizing changes in the LSM solution across frequency [5]. We hypothesize that we can achieve additional imaging improvements by suppressing artifacts that do not evince the correct phase delay differences corresponding to their spatial locations relative to the array.

We apply the proposed technique to simulated sparse aperture scattered field data from several example complex targets. The results show that the phase-delay-based frequency variation constraint significantly improves imaging fidelity as compared to both the standard multifrequency LSM as well as a frequency-variation regularized LSM that neglects the phase-delay constraint. The proposed technique is more robust to sensor placement and results in significantly fewer imaging artifacts, at the expense of a modestly higher degree of blurring of target boundaries in some instances resulting from imperfections of the phase assumption for resonant target features.

2.2 Imaging Formulation

2.2.1 Imaging Scenario and Conventional Formulation

We assume an imaging scenario wherein an unknown target of interest with spatial support V is surrounded by an array of N_{tx} transmitters and N_{rec} receivers. Each transmitter sequentially illuminates the imaging scene with an incident electric field, and the resulting scattered field is recorded by each receiver. At each frequency of interest, the scattered field phasors are collected in an $N_{\mathrm{rec}} \times N_{\mathrm{tx}}$ matrix $\mathbf{E}(k)$, where k represents the wavenumber at the frequency of interest. We assume two-dimensional transverse magnetic propagation for convenience, and thus each element of $\mathbf{E}(k)$ is a complex scalar. The standard single-frequency LSM is performed by finding a solution to the following inverse problem at each pixel of interest:

$$\mathbf{E}(k)\mathbf{g}(k,\mathbf{r}) = \mathbf{\Phi}(k,\mathbf{r}) \tag{1}$$

In (1), $\mathbf{\Phi}(k,\mathbf{r})$ is an $N_{\mathrm{rec}} \times 1$ vector containing the Green's function between pixel location $\mathbf{r}$ and each receiver location and $\mathbf{g}(k,\mathbf{r})$ is an $N_{\mathrm{tx}} \times 1$ vector of complex weights to be solved for. Assuming full-aperture data, a bounded-norm solution for $\mathbf{g}(k,\mathbf{r})$ can be found if $\mathbf{r}$ is within the support of the target. If $\mathbf{r}$ is outside the target support or at the boundary, the solution is unbounded [1]. A multifrequency image of the target support may be created after forming $\mathbf{g}(k,\mathbf{r})$ for each k of interest by displaying an indicator function given by

$$I(\mathbf{r}) = \sum_k \|\mathbf{g}(k,\mathbf{r})\|^{-1}, \tag{2}$$

which will be large for points inside the target and small for points outside the target.

The inverse problem (1) is ill-posed, and thus susceptible to non-unique solutions. This problem is exacerbated if **E**(*k*) is sparsely sampled. In the following subsection, we lay out the formulation for a technique to reduce reconstruction aberrance in these scenarios via the incorporation of *a priori* phase relationships between frequencies.

2.2.2 Proposed Formulation

We derive the proposed constraint to the LSM solution by first noting that a **g**(*k*,**r**) satisfying (1) must also satisfy

$$\mathbf{\Phi}^{\mathrm{H}}(k,\mathbf{r})\mathbf{E}(k)\mathbf{g}(k,\mathbf{r}) = \|\mathbf{\Phi}(k,\mathbf{r})\|^2, \tag{3}$$

where 'H' denotes the conjugate transpose. The product of the Green's function and the scattered field on the left side of (3) can be expressed in integral equation form via

$$\mathbf{\Phi}^{\mathrm{H}}(k,\mathbf{r})\mathbf{E}(k) = jk\eta \int_V \mathbf{\Phi}^{\mathrm{H}}(k,\mathbf{r})\,\mathbf{\Phi}(k,\mathbf{r}')\mathbf{J}^{\mathrm{T}}(k,\mathbf{r}')d\mathbf{r}' \tag{4}$$

where $\mathbf{J}(k,\mathbf{r}')$is the $N_{\mathrm{tx}} \times 1$ vector of currents induced at point **r**' in *V* via the incident electric fields radiated from each transmitter, 'T' denotes the transpose, and η is the impedance of the background. The product of the two Green's functions in (4) is essentially a matched filter for the receive array. Assuming sufficient spatial resolution of the matched filter, we can expect the integral to be dominated by the contribution of the current distribution in the vicinity of **r**'=**r**.

If the Born approximation is valid, we can assume that the phase of $\mathbf{J}(k,\mathbf{r}')$ is primarily determined by the electrical length traversed by the incident electric field between the transmitters and **r**. We can therefore write

$$\mathbf{J}(k,\mathbf{r}) \approx \mathbf{J}(k+\Delta k,\mathbf{r}) \odot \exp\big(j\Delta k\mathbf{d}(\mathbf{r})\big), \tag{5}$$

where **d**(**r**) is an $N_{\mathrm{tx}} \times 1$ vector of distances between each transmit location and **r**, Δk is a small wavenumber step, '$\odot$' denotes pointwise multiplication, and we have neglected amplitude decay of the incident wave. Using (3)-(5), and neglecting amplitude effects, we can state the following assumption on the LSM solution at closely spaced frequencies:

$$\mathbf{g}(k,\mathbf{r}) \approx \mathbf{g}(k+\Delta k,\mathbf{r}) \odot \exp\big(j\Delta k\mathbf{d}(\mathbf{r})\big) \tag{6}$$

We wish to enforce (6) as a constraint (or, equivalently, as a penalty term) on the multifrequency LSM solution. We therefore perform the LSM inversion using the following Tikhonov-regularization-based minimization at every point **r**:

$$\min_{\mathbf{g}(k)} \sum_{k} \|\mathbf{E}(k)\mathbf{g}(k) - \mathbf{\Phi}(k)\|^2 + \alpha\|\mathbf{g}(k)\|^2 + \beta D(k) \tag{7}$$

In (7), α and β are regularization parameters, we have neglected the **r**-dependence of **g**, **Φ**, and **D** for convenience, the norms are L_2, and

$$D(k) = \|\mathbf{g}(k) - \mathbf{g}(k + \Delta k) \odot \exp(j\Delta k\mathbf{d})\|^2 \tag{8}$$

Setting $\beta = 0$ in (7) results in a conventional Tikhonov-regularized multifrequency LSM optimization, while setting $\beta > 0$ penalizes LSM solutions that deviate from the desired phase relationship given in (6). Calculation of the solution to (7) can be performed via a convenient block-matrix implementation in a similar manner as is described in [5]. In the remainder of this section, we investigate the effectiveness of the proposed technique using simulated data.

2.3 Simulated Data Acquisitions

We acquire simulated scattered field data via two-dimensional finite-difference time-domain (FDTD) simulations. Scattered field data from each simulation are collected in the time domain and then transformed to the frequency domain via discrete Fourier transform. Data are recorded in this manner for 51 uniform wavenumber steps spanning the band $[0.33\ 1.66]2\pi/\lambda_c$, where λ_c is the wavelength at the center of the band.

We choose two target scenes whose support is illustrated in Fig. 1. The background medium in each case is free space, and the relative permittivity of each target is set at 2. The maximum target extent as measured from scene center ranges from λ_c to $1.5\lambda_c$.

Transmit and receive locations are placed on a ring encircling the target with radius $6\lambda_c$. We choose $N_{\mathrm{tx}} = 45$ equally spaced transmit locations in order to satisfy the spatial Nyquist criterion [6] $N_{\mathrm{tx}} > 2k_{\mathrm{max}}a$ for the maximum wavenumber in the recorded bandwidth $k_{\mathrm{max}} = 1.66(2\pi/\lambda_c)$ and a modestly overestimated maximum scene extent of $a = 2\lambda_c$. The electric field is launched at each transmit location via an elementary current source.

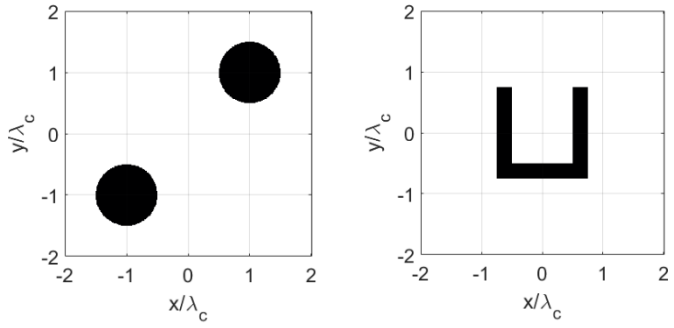

Fig. 1 - Support for the two targets used in this study. Black indicates the target support, while white indicates background.

We investigate the use of two different sparse sets of receive locations, which are listed in Table I. Receiver angles are measured counterclockwise from the +*x*-axis. In Receiver Set A, we use $N_{\mathrm{rec}} =$

6equally spaced receivers. In Receiver Set B, we set $N_{\text{rec}} = 4$ and assume that we are constrained to cluster the receivers around only three of the four cardinal directions.

Following data collection, we corrupt the recorded data with Gaussian white noise. The noise is scaled such that the signal to noise ratio (defined here as the ratio of total signal power across all recorded signal samples to the total noise power across all samples) is 50 dB.

Table 1 - Receiver placement

Receiver Set	Receiver angles
A	0º, 60º, 120º, 180º, 240º, 300º
B	0º, 90º±5º, 180º

2.4 Results and Discussion

In this subsection, we report the results of applying the proposed phase-delay-based frequency variation (PDFV) formulation of the LSM to the simulated data sets. We also report imaging results from both the standard multifrequency LSM as well as a frequency variation (FV) implementation of LSM that follows the same form as (7) and (8) with the phase-delay relationship neglected, i.e., the complex exponential term in (8) is replaced with a vector of ones. The FV technique used here differs from the one presented in [5] in that an L_2 norm is minimized in (8) instead of an L_1 norm. However, comparing PDFV results to FV results using the L_2 formulation allows us to directly evaluate the degree to which the phase-delay constraint improves imaging performance as compared to the degree to which the improvement comes from constraining overall changes in $\mathbf{g}(k)$. Across all data sets, we use regularization parameters $\alpha = 1 \times 10^{-6}$and $\beta = 1 \times 10^{-1}$.

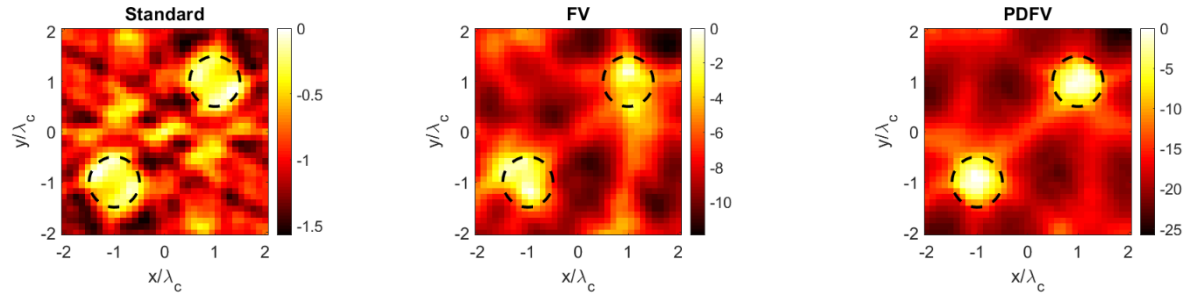

Fig. 2 - LSM image results for Receiver Set A for the first target scene. Colorbar values correspond to $\mathbf{20\log_{10} \boldsymbol{I}(\mathbf{r})}$, referenced to the maximum value in each image.

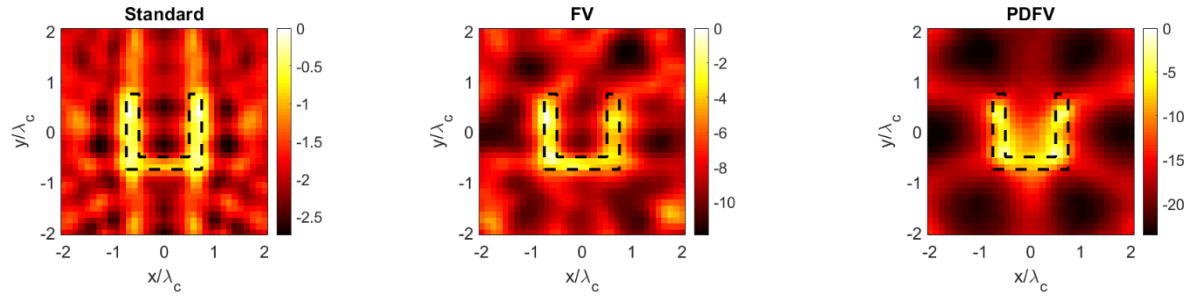

Fig. 3 - LSM image results for Receiver Set A for the second target scene. Colorbar values correspond to $\mathbf{20\log_{10} \boldsymbol{I}(\mathbf{r})}$, referenced to the maximum value in each image.

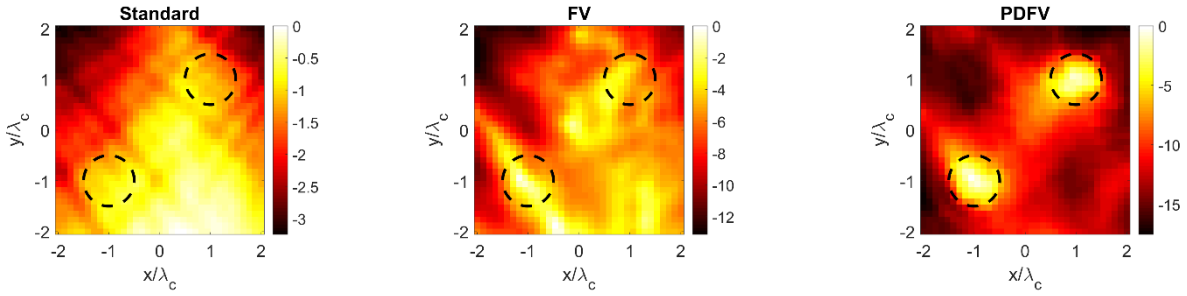

Fig. 4 - LSM image results for Receiver Set B for the first target scene. Colorbar values correspond to $\mathbf{20\log_{10} \boldsymbol{I}(\mathbf{r})}$, referenced to the maximum value in each image.

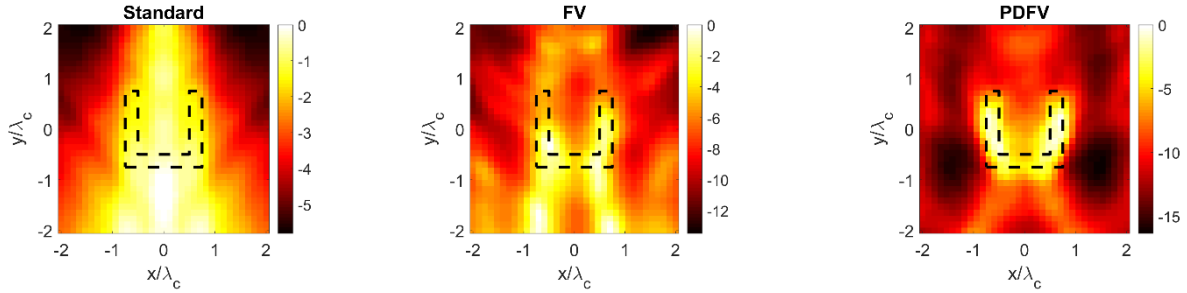

Fig. 5 - LSM image results for Receiver Set B for the second target scene. Colorbar values correspond to $\mathbf{20\log_{10} \boldsymbol{I}(\mathbf{r})}$, referenced to the maximum value in each image.

Image results for Receiver Set A are shown in Figs. 2-3. Significant artifacts are present in the standard LSM images for both targets due to the sparsely sampled receive aperture. The artifacts are reduced in the FV LSM images, especially in the close vicinity of the targets. However, there are still significant artifacts near the edges of the imaging scene. The PDFV images show further reduction in artifacts compared to the FV images. The reconstructed shapes of the two circular targets in Fig. 2 are also more faithfully rendered in the PDFV image compared to the FV image. In Fig. 3, the PDFV image of the U-shaped target exhibits a modest degree of blurring in its cavity. This may be due to multipath effects that are not captured by the phase-delay constraint. Still, the reconstruction evinces the concave nature of the true target with significantly reduced artifacts.

Image results for Receiver Set B are shown in Figs. 4-5. The standard and FV LSM solutions for these cases are both extremely aberrant, in that the images completely fail to recover the true shapes of each targets. In contrast, the PDFV results achieve a high degree of fidelity.

The results demonstrate the promise of the phase-delay-based frequency variation constraint for LSM imaging with sparsely sampled apertures. Further analysis is required to fully characterize the limits of the technique. While the Born approximation simplified our analysis in Sec. II, it remains to be seen how critical it is to imaging performance, especially for small frequency steps. Strategies for choosing regularization parameters α and β must also be studied. The technique must be applied to experimental data and data from three-dimensional scattering scenes.

Techniques for improving performance will also be a subject of future study. As currently implemented, the penalty term $D(k)$ in (8) changes for every pixel in the imaging scene, which increases computational expense compared to other LSM formulations. Future work will involve modifying the formulation to allow for parallelization.

2.5 Summary

In this section, we introduced a formulation of the multifrequency Linear Sampling Method for sparse aperture imaging scenarios. We applied a frequency variation constraint that encourages the phase of the solution at each pixel to correspond to the expected propagation-based phase delay between the

pixel location and the imaging array. Using simulated data, we showed that the proposed technique significantly improves imaging performance in sparse aperture scenarios by suppressing artifacts that don't evince the correct phase delays for their spatial positions. In several cases, the improvement in performance is significant enough that the true target shape is easily identifiable in the images from the proposed technique while being completely unidentifiable in images from the standard technique. Future work will build upon the results of this study to characterize the limits of the technique, demonstrate experimental imaging, and improve parallelizability.

3. A FAR-FIELD TRANSFORMATION PROCEDURE FOR MONOSTATIC LINEAR SAMPLING METHOD IMAGING

This section is adapted from a paper published in the 2019 Proceedings of International Conference on Electromagnetics in Advanced Applications [7].

3.1 Background

To date, research works dedicated to treatment of sparse aperture qualitative inverse scattering have been rather sparse. Of the few works that have addressed this problem, there have been approaches that rely on incorporating multifrequency information either in the native frequency domain [8] or from a time-domain perspective [9]. Others such as [10] introduced more sophisticated regularization schemes that attempted to leverage additional priors from multispectral data. However, all of these approaches would also fail when the transmit aperture is also sparse. What has been lacking in the literature are studies where the LSM can exploit the highly redundant nature of multistatic data prior to inversion. Some examples of multistatic enrichment procedures have been presented in previous works such as in [11], where a pseudo total-variation scheme was considered, however we argue the use of schemes such as total variation or Tikhonov for enrichment are local techniques that do not specifically leverage the fact that dense multistatic data is somehow low-dimensional.

In this paper we take a different approach towards an enrichment algorithm for qualitative inverse scattering with the specific case of imaging from monostatic geometries. Our approach is a two-step procedure that is based on exploiting multistatic redundancy from a K-space perspective. In the first step we find regions where the support of monostatic and bistatic geometries intersect in K-space, which are then used to fill in the missing data points. The second step aims to complete the remainder of the bistatic apertures for which there is no intersection with monostatic support using a matrix completion procedure [12].

3.2 Preliminaries

For the sake of simplicity we restrict ourselves to $\mathbb{R}^2$ in this work. Assume a homogeneous background medium embedding extended targets with reflectivity $\rho(\boldsymbol{x})$ and whose support $\Sigma \subset \mathbb{R}^2$ is compact with connected boundary Γ. Let S denote the unit circle and let $u^i(\boldsymbol{x};\widehat{\boldsymbol{d}})$ represent an interrogating monochromatic planewave traveling in a direction $\widehat{\boldsymbol{d}} \subset S$ with wavenumber $k > 0$. The incident field induces a scattered field $u^s(\boldsymbol{x})$ for which the total field satisfies

$$\nabla^2 u(\boldsymbol{x}) + k^2 n(\boldsymbol{x}) = 0, \text{for } x \in \mathbb{R}^2 \backslash \Gamma \tag{9}$$

$$u(\boldsymbol{x}) = u^i(\boldsymbol{x};\widehat{\boldsymbol{d}}) + u^s(\boldsymbol{x}) \tag{10}$$

$$\lim_{r\to\infty} \sqrt{r}\left(\frac{\partial u^s}{\partial r} - iku^s\right) = 0, r = |\boldsymbol{x}| \tag{11}$$

Here $n(\boldsymbol{x})$ is the index of refraction which assumes the form $n(\boldsymbol{x}) = 1 - \rho(\boldsymbol{x})$. The total field $u(\boldsymbol{x})$ (in most reasonable cases) can be represented in the form of a Lippmann-Schwinger integral,

$$u(\boldsymbol{x}) = u^i(\boldsymbol{x}; \widehat{\boldsymbol{d}}) - k^2 \int_{\mathbb{R}^2} G(\boldsymbol{x}, \boldsymbol{y}) \rho(\boldsymbol{y}) u(\boldsymbol{y}) d^2 y, \text{for } x \in \mathbb{R}^2 , \tag{12}$$

where we have the homogeneous Green's function defined as

$$G(\boldsymbol{x}, \boldsymbol{y}) = \frac{i}{4} H_0^1(k|\boldsymbol{x} - \boldsymbol{y}|). \tag{13}$$

Writing (12) in operator form we can compactly write the forward problem as

$$\left(I + k^2 A_\rho\right)^{-1} u(\boldsymbol{x}) = u^i(\boldsymbol{x}; \widehat{\boldsymbol{d}}), \tag{14}$$

where we have defined

$$A_\rho f(\boldsymbol{x}) \coloneqq \int_{\mathbb{R}^2} G(\boldsymbol{x}, \boldsymbol{y}) \rho(\boldsymbol{y}) f(\boldsymbol{y}) d^2 y. \tag{15}$$

The forward problem being well-posed [13] allows us to write

$$u(\boldsymbol{x}) = \left(I + k^2 A_\rho\right)^{-1} u^i(\boldsymbol{x}; \widehat{\boldsymbol{d}}). \tag{16}$$

The inverse scattering problem is to recover $\rho(\boldsymbol{x})$ from knowledge of the scattered field $u_s(\boldsymbol{x})$. Under the condition that $\|A_\rho\| < 1$, we can expand the inversion operator in (16) into a Neumann series [14]

$$u(\boldsymbol{x}) = \left(I - k^2 A_\rho + k^4 A_\rho^2 - k^6 A_\rho^3 + \cdots\right) u^i(\boldsymbol{x}; \widehat{\boldsymbol{d}}). \tag{17}$$

From (17) we can see that although the mapping between u and u^i is linear, it is nonlinear between u, (and equivalently u^s) and ρ. The Born approximation, being a so called weak scattering relaxation, dictates that only the first two terms in the expansion (17) is relevant which effectively linearizes the inverse problem. Thus retaining only the first two terms in (17) and then subtracting out the incident field from the equation we obtain a linear relationship between ρ and u^s,

$$u^s(\boldsymbol{x}) = -k^2 \int_{\mathbb{R}^2} G(\boldsymbol{x}, \boldsymbol{y}) \rho(\boldsymbol{y}) u(\boldsymbol{y}) d^2 y. \tag{18}$$

In the far-field where as $r \to \infty$ we have that $u^s(\boldsymbol{x}, \widehat{\boldsymbol{d}})$ asymptotically approaches its corresponding far-field pattern $u_\infty^s(\widehat{\boldsymbol{x}}, \widehat{\boldsymbol{y}})$ and

$$G(\boldsymbol{x}, \boldsymbol{y}) \longrightarrow G_\infty(\widehat{\boldsymbol{x}}, \boldsymbol{y}) = \frac{e^{\frac{i\pi}{4}}}{\sqrt{8\pi k}} e^{-ik\widehat{\boldsymbol{x}}.\boldsymbol{y}}. \tag{19}$$

Therefore in the far-field we have

$$u_\infty^s(\widehat{\boldsymbol{x}}, \widehat{\boldsymbol{y}}) = -\gamma \int_{\mathbb{R}^2} e^{-ik(\widehat{\boldsymbol{x}} - \widehat{\boldsymbol{d}}).\boldsymbol{y}} \rho(\boldsymbol{y}) d^2 \boldsymbol{y}, \tag{20}$$

with

$$\gamma = \frac{k^2 e^{\frac{i\pi}{4}}}{\sqrt{8\pi k}}. \tag{21}$$

the spatial frequencies (knots) as $\boldsymbol{k} = k(\hat{\boldsymbol{x}} - \hat{\boldsymbol{d}})$ we obtain a Fourier relationship between the image and the Born approximated scattered field,

$$u_\infty^{\mathrm{BA}} = -\gamma \int_{\mathbb{R}^2} e^{-i\boldsymbol{k}.\boldsymbol{y}} \rho(\boldsymbol{y}) d^2\boldsymbol{y}. \tag{22}$$

Conventional back-projection imaging is based on applying an inverse Fourier transform onto the scatter data to retrieve $\rho(\cdot)$.

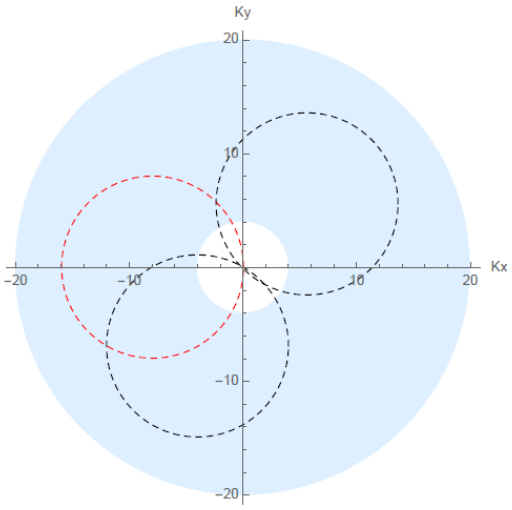

Fig. 6 - Here we have an example of a full aperture monostatic region R for $k_{\min} = 2$ and $k_{\max} = 10$ which is shaded in light blue. The dashed lines correspond to bistatic regions C_p for $k_p = 8$, and 3 different incident angles. The white region contains spatial frequencies not captured by the monostatic geometry.

3.2.1 Review of the LSM

Qualitative imaging methods, like the LSM, take a different point of view of the inverse problem, where we aim to reconstruct the support Σ rather than $\rho(\cdot)$ itself from the scattered data. A brief description of the LSM begins with defining the far-field operator $F: L^2(S) \to S$,

$$Fg(\hat{\boldsymbol{x}}) := \int_S u_\infty^s(\hat{\boldsymbol{x}}, \hat{\boldsymbol{d}})\, g(\hat{\boldsymbol{d}}) ds(\hat{\boldsymbol{d}}). \tag{23}$$

Our aim is to find a weight function $g(\hat{\boldsymbol{d}}, \boldsymbol{z}) \in L^2(S)$ so that the field resulting from application of (23) coincides with the far-field of a radiating point source located at $\boldsymbol{z} \in \Sigma$. In other words we aim to find a solution to the far-field equation

$$Fg(\hat{\boldsymbol{x}}, \hat{\boldsymbol{z}}) = G_\infty(\hat{\boldsymbol{x}}, \hat{\boldsymbol{z}}). \tag{24}$$

It can be shown [15] that for any $\epsilon > 0$ there always exists a density within ϵ distance of the point source which remains bounded whenever $\boldsymbol{z} \in \Sigma$. As $\boldsymbol{z} \to \Gamma$ any such approximating solution has the asymptotic behavior $\|g\|_{L^2(S)} \to \infty$ and remains unbounded for all $\boldsymbol{z} \in \Sigma^+$. In this sense $\|g(\cdot, \boldsymbol{z})\|_{L^2(S)}$ forms the basis of an indicator function for the set Σ. Practical application of the technique however relies on a regularization solution to (15). The conventional approach is through Tikhonov regularization

$$\min_{\|g(\cdot,\boldsymbol{z},k)\in L^2(S)\|} \|Fg - G_\infty\|^2_{L^2(S)} + \alpha\|g\|^2_{L^2(S)} \tag{25}$$

which is strictly convex for any $\alpha > 0$. There are a number of advantages for employing the Tikhonov approach; first we can explicitly prove that this particular regularization scheme admits solutions that adhere to the properties we outlined above [16], and secondly the solution can be computed in a rather efficient manner. We refer readers to section 3.1 of [10] for a discussion of an efficient numerical block-wise approach for Tikhonov based LSM.

3.3 Monostatic to Multistatic Transformation

From (16) we can see that a major drawback to the LSM is the need to know $u^S_\infty(\cdot,\cdot)$ for all $(\hat{\boldsymbol{x}}, \hat{\boldsymbol{d}}) \in S \times S$, which is a considerable amount of spatial data. It is well known that when the data consists of only a few bistatic pairs the LSM fails [17], and cannot even be applied with monostatic data in its native form. However it is also well known that complete multi-static knowledge is overly redundant when frequency diversity is available, which is usually much easier to achieve in most applications.

Furthermore dense monostatic data over a band $B = [k_{\min}, k_{\max}]$ should contain enough information to image a scene in stable fashion, although again it is not clear how techniques like LSM can leverage it. The spatial frequency representation of the data gives us perspective on how monostatic and multi-static geometries are related in terms of information overlap. In the monostatic case, the knots reduce to $\boldsymbol{k} = 2k\hat{\boldsymbol{k}}$, which means that the region of support is contained in an annular region R centered at the origin as shown in Fig. 6. Now consider a single bistatic configuration with a fixed direction of incidence $\hat{\boldsymbol{d}}$ and fixed wavenumber $k_p \in (k_{\min}, k_{\max}]$. We see from Fig. 6 that the aperture traces out a circle C_p (also known as an Ewald sphere [14]) centered at $k_p\hat{\boldsymbol{d}}$ with radius k_p. We can also observe that there is a segment of C_p contained in R while the remainder of bistatic aperture is outside the monostatic region of support. In fact this holds for all $\hat{\boldsymbol{d}} \in S$ and for any $k_p \in (k_{\min}, k_{\max})$. The strategy is then clear; given monostatic data on a band B, we aim to construct a virtual multistatic data set by filling in values on regions where the two coincide. As we can see in Fig. 6 this will yield data on a continuous portion of the aperture, while the remainder still remains unknown. However under mild assumptions on Σ the far-field data u^S_∞ is analytic [18] thus for any $\hat{\boldsymbol{d}}$ and k_p we can uniquely extend this function onto the entire aperture as justified by the principle of analytic continuation.

3.3.1 Far-Field Aperture Completion

The problem of extending $u_\infty(\hat{\boldsymbol{x}}, \hat{\boldsymbol{d}})$ for fixed $\hat{\boldsymbol{d}}$ and $k > 0$ onto the entire aperture S given knowledge of u_∞ on a continuous subset of S is known to be ill-posed. Previous works such as [19] use techniques such as Tikhonov or TV to regularize the inverse problem. However we argue that these techniques have only a local point of view of the data and do not exploit multistatic redundancy as a prior. Instead we look at the problem from the discrete perspective of matrix completion. In matrix completion [12] one seeks to predicting/recover missing values of a matrix given the values of a small subset of known entries. The problem of course is highly ill-posed however, it has been shown that if the underlying matrix is sufficiently low-rank it can be recovered surprisingly accurately using a rather small number of known entries [12]. Furthermore recovery of the matrix can be accomplished in polynomial time using convex

optimization. To be more specific, let $\boldsymbol{X} \in \mathbb{C}^{n\times n}$ be a matrix and $P: \mathbb{C}^{n\times n} \to \mathbb{C}^{m\times 1}$ be the linear map that extracts the known *m* entries of $\boldsymbol{X}$. We then seek to find a solution

$$\min_{\boldsymbol{X}\in\mathbb{C}^{n\times n}} \{\text{rank}(\boldsymbol{X}) : \|P(\boldsymbol{X}) - b\|_2 < \epsilon\}. \tag{26}$$

While solving (26) is known to be NP-hard, a convex relaxation via the nuclear norm can be solved in polynomial time and under mild conditions can achieve an equivalent solution to (26). Therefore we seek instead to solve

$$\min_{\boldsymbol{X}\in\mathbb{C}^{n\times n}} \{\|\boldsymbol{X}\|_{1,*} : P(\boldsymbol{X}) = b\} \tag{27}$$

with the nuclear norm defined as

$$\sum_{i=1}^{n} \sigma_i(\boldsymbol{X}), \tag{28}$$

And the $\sigma_i(\boldsymbol{X})$'s are the singular values of $\boldsymbol{X}$.

3.3.2 Discretized Numerical Approach

We now describe our numerical approach in more concrete terms. Given monostatic data at the spatial frequencies $\boldsymbol{k}_i$, which we assume are sampled sufficiently for the underlying scene, we interpolate the sampled data to obtain a model of $u_\infty^{\text{BA}}(\boldsymbol{k})$ for all $\hat{\boldsymbol{k}} \in R$. Next we construct a $n \times n$ multistatic grid $(\hat{\boldsymbol{x}}_i, \hat{\boldsymbol{d}}_j)$, where $\hat{\boldsymbol{x}}_i$ and $\hat{\boldsymbol{d}}_j$ are the *i*th bistatic observation direction due to a planewave from the *j*th direction, for a chosen wavenumber $k_p \in (k_{\text{min}}, k_{\text{max}})$. These grid points will then correspond to a $n \times n$ multistatic response matrix $\boldsymbol{F}$ whose entries would ideally be given as

$$F_{ij} = u_\infty^S(\hat{\boldsymbol{x}}_i, \hat{\boldsymbol{d}}_j). \tag{29}$$

Let $\mathfrak{T}$ denote the index set $\{1,2,\dots,n\}$ and define the set of spatial frequencies

$$\mathcal{S} = \{\boldsymbol{k}_{i,j'} \in R: \boldsymbol{k}_{i',j'} = k_p(\hat{\boldsymbol{x}}_{i'} - \hat{\boldsymbol{d}}_{j'}), (i',j') \in \mathfrak{T}\times\mathfrak{T}\}. \tag{30}$$

Now let the index set $\mathcal{J} = 1,\dots,m = |\mathcal{S}|$ enumerate the set $\mathcal{S}$, for which we can define the mapping $P: \boldsymbol{F} \mapsto \boldsymbol{b}$ where $\boldsymbol{b} \in \mathbb{C}^m$ is defined component-wise as

$$b_j = u_\infty^{\text{BA}}(\boldsymbol{k}_j), \text{for } j \in \mathcal{J}. \tag{31}$$

Then for a defined tolerance $\epsilon > 0$ we complete the matrix $\boldsymbol{F}$ for the remainder of the entries via solving (27). In this work we employ an accelerated proximal gradient (APG) approach similar in nature to the method employed in [20], the details of which we leave for a future paper.

3.4 Simulation Results

We present some imaging results to evaluate efficacy for the described monostatic LSM approach. For the first experiment we consider a simple perfectly conducting kite shaped target. For this scene we simulated far-field scatter data corresponding to a low-frequency monostatic collection using a method of moments (MoM) code. The monostatic geometry was obtained at 1 degree increments for a band of

frequencies corresponding to wavenumbers $k_{min} = 2$ and $k_{max} = 10$. For the virtual multistatic response data, we chose a grid of incident and observation directions both sampled in 1 degree increments, and set the desired wavenumber as $k_p = 6$. Fig. 7 shows the simulated monostatic response, the virtual multistatic response corresponding to $k_p = 6$ as obtained by our transformation procedure, and the associated LSM reconstruction obtained via Tikhonov regularization.

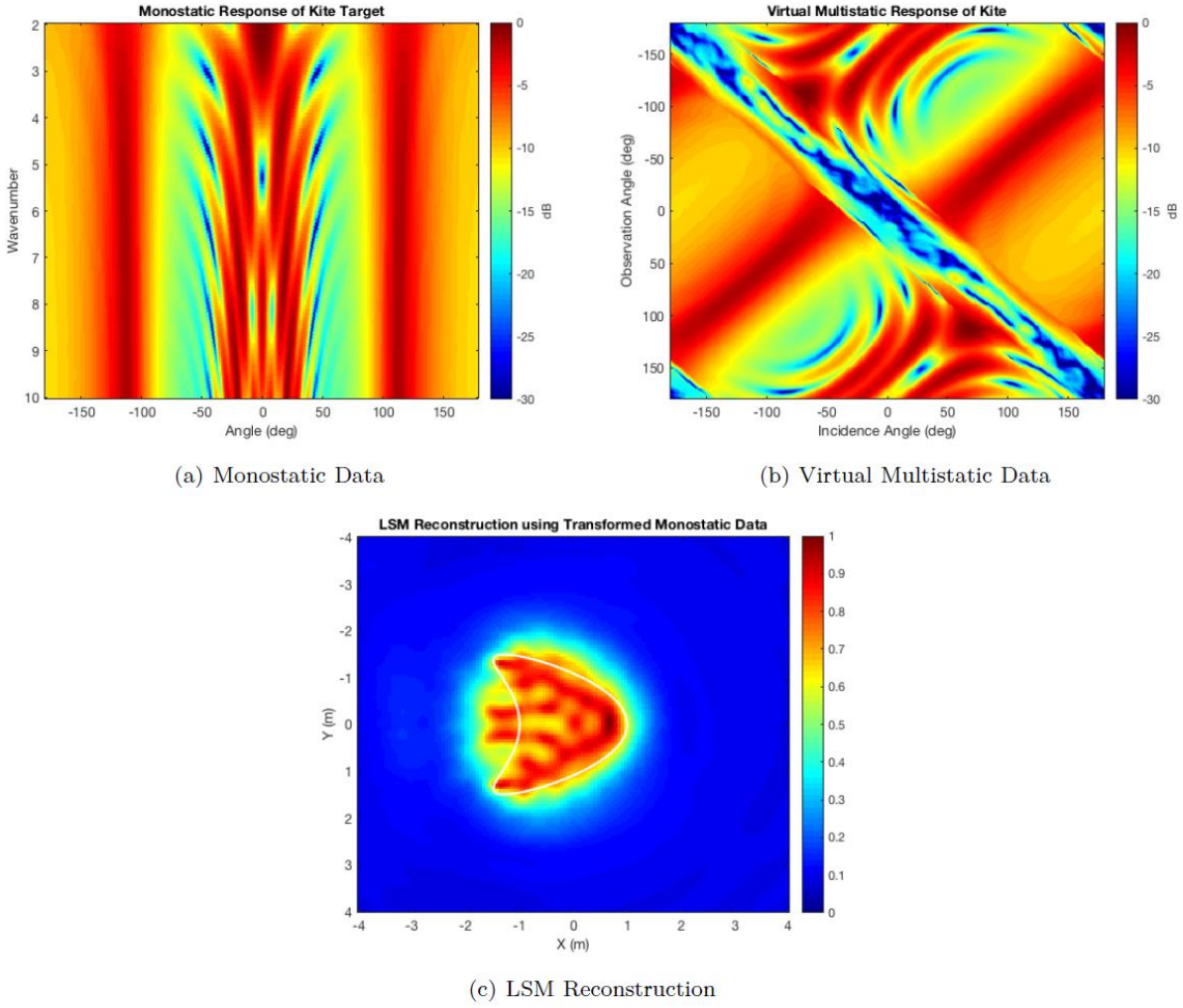

(a) Monostatic Data

(b) Virtual Multistatic Data

(c) LSM Reconstruction

Fig. 7 - Results for a simple example of imaging a kite PEC scatterer, a) simulated monostatic data of the kite across angle and frequency. b) Virtual multistatic data corresponding to a single wavenumber $k_p = 6$ using 1 degree sampling in both observation and incidence. c) The resulting LSM reconstruction.

For the second experiment we consider 2D monostatic scatter data taken from a detailed simulation [21] of the DJI Phantom II quadcopter target. The scatter data was obtained by FDTD code developed at ARL where the monostatic response was measured again at every 1 degree over a 1-10 GHz range, which corresponded to approximately to $k_{min} = 21$ and $k_{max} = 209$. Looking at the HH monostatic response of the quadcopter target in Fig. 8, we note that the data does not exhibit as much symmetry as the kite's monostatic response. For our LSM reconstruction we chose $k_p = 170$ and as before sampled both incidence and observation apertures using 1 degree increments. The resulting reconstruction of the quadcopter is also shown in Fig. 8.

3.5 Summary and Future Work

To summarize, in this paper we presented an enrichment procedure which mapped dense monostatic data into a virtual multistatic data for the purpose of applying LSM based imaging when only monostatic data is available. As discussed the procedure was based on finding spatial frequency regions of common support which was then followed by a matrix completion algorithm to extend the predicted data onto the entire multistatic apertures. There are several clear paths of future extensions of this work. Firstly incorporating all frequencies simultaneously instead of enrichment on a single frequency basis. Secondly extension of the approach to the full 3D and polarimetric LSM framework remains to be investigated. More fundamentally however, while the simulations given here do indicate initial efficacy of the approach, several questions still remain as we note that the argument behind the presented procedure is only valid under the Born approximation, which goes against one of the main arguments for using the LSM in the first place. Therefore as future work it would be interesting to compare the LSM reconstructions using the procedure using data for which the Born approximation is satisfied as well as images obtained using conventional backprojection. However more importantly the work here lays the foundation for an enrichment procedure for when some bistatic data is known and needs to be extended to denser multistatic grids. In this case we anticipate the procedure would be very similar to what we described here, and that reliance on the Born approximation should be less of an issue.

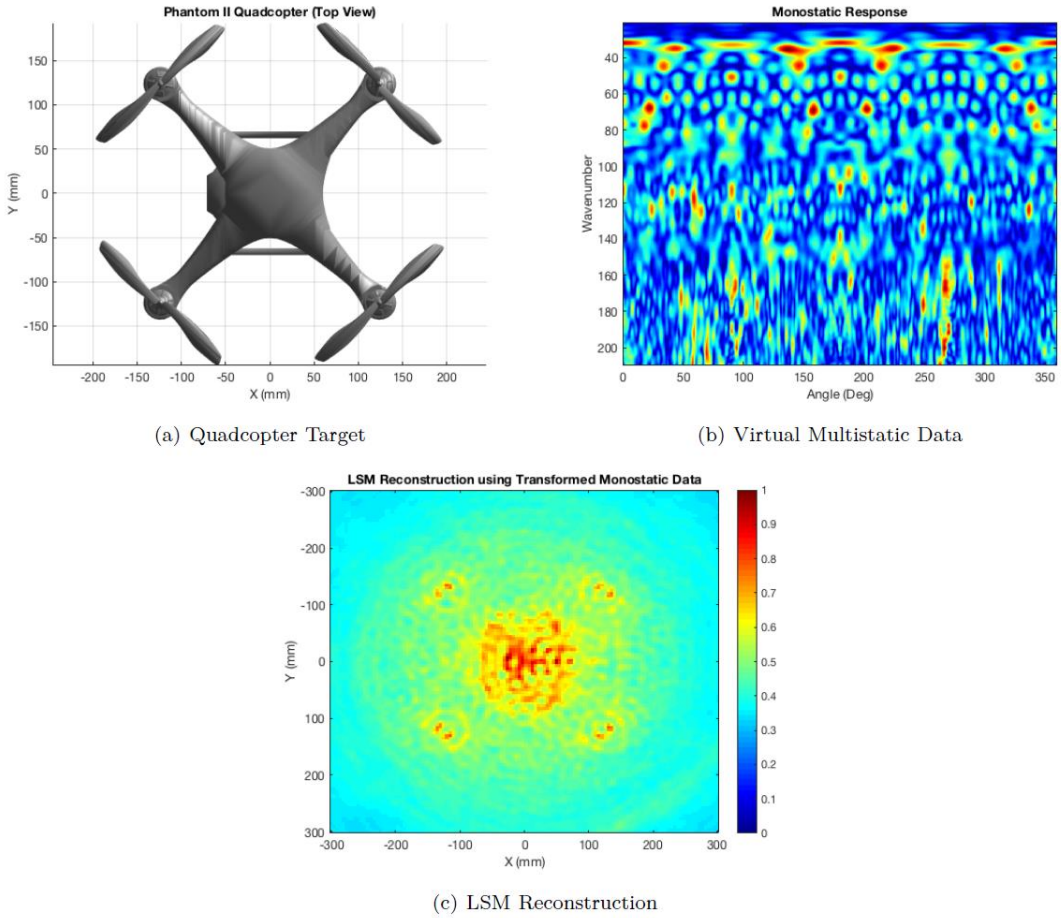

(a) Quadcopter Target

(b) Virtual Multistatic Data

(c) LSM Reconstruction

Fig. 8 - Reconstruction of the DJI Phantom quadcopter target a) A 3D model of the quadcopter oriented in the same direction as was used in the 2D FDTD simulation. b) The monostatic response in terms of wavenumber and angle. c) LSM reconstruction using the virtual multistatic data at virtual wavenumber k_p = 170 and 1 degree sampling in both observation and incidence.

REFERENCES

[1] F. Cakoni, D. Colton and P. Monk, The Linear Sampling Method in Inverse Scattering Theory, Philadelphia, PA: Society for Industry and Applied Mathematics, 2011.

[2] M. Burfeindt and H. Alqadah, "Sparse-aperture qualitative inverse scattering using a phase-delay-based frequency variation constraint," in *IEEE Research and Applications of Photonics in Defense*, Miramar Beach, FL, 2019.

[3] Y. Guo, D. Colton and P. Monk, "Toward a Time Domain Approach to the Linear Sampling Method," *Inverse Problems,* vol. 29, no. 9, p. 095016, 2013.

[4] H. Alqadah and N. Valdivia, "3D Shape Reconstruction Using a Novel Multi-Frequency Linear Sampling Method Predictor," in *International Conference on Electromagnetic Advanced Applications*, 2014.

[5] H. Alqadah, "A Compressive Multi-Frequency Linear Sampling Method for Underwater Acoustic Imaging," *IEEE Transactions on Image Processing,* vol. 25, no. 6, pp. 2444-2455, 2016.

[6] O. Bucci and G. Franceschetti, "On the Spatial Bandwidth of the Scattered Field," *IEEE Transactions on Antennas and Propagation,* Vols. AP-35, no. 12, pp. 1445-1455, 1987.

[7] H. Alqadah and M. Burfeindt, "A Far-Field Transformation Procedure for Monostatic Linear Sampling Method Imaging," in *International Conference on Electromagnetics in Advanced Applications*, Granada, Spain, 2019.

[8] F. Cakoni and D. Colton, "On the Determination of Dirichlet and Transmission Eigenvalues from Far Field Data," *Comptes Rendus Mathematique,* vol. 348, pp. 379-383, 2010.

[9] Q. Chen, H. Haddar, A. Lechleiter and P. Monk, "A Sampling Method for Inverse Scattering in the Time Domain," *Inverse Problems,* vol. 26, p. 085001, 2010.

[10] H. Alqadah and N. Valdivia, "A Frequency Based Constraint for a Multi-Frequency Linear Sampling Method," *Inverse Problems,* vol. 29, no. 9, p. 095019, 2013.

[11] A. Barucq, C. Bekley and R. Djellouli, "A Multi-Step Procedure for Enriching Limited Two-Dimensional Acoustic Far-Field Pattern Measurements," *Journal of Inverse and Ill-Posed Problems,* vol. 18, pp. 189-216, 2010.

[12] E. Candes and B. Recht, "Exact Matrix Completion via Convex Optimization," *Foundations of Computational Mathematics,* vol. 9, p. 717, 2009.

[13] W. McLean, Strongly Elliptic Systems and Boundary Integral Equations, Cambridge University Press, 2000.

[14] A. Devaney, Mathematical Foundations of Imaging, Tomography, and Wavefield Inversion, Cambridge University Press, 2012.

[15] F. Cakoni and D. Colton, "On the Mathematical Basis of the Linear Sampling Method," *Georgian Math Journal,* vol. 10, pp. 95-104, 2003.

[16] T. Arens and A. Lechleiter, "The Linear Sampling Method Revisited," *Journal of Integral Equations and Applications,* vol. 21, pp. 179-202, 2009.

[17] H. Alqadah, N. Valdivia and E. Williams, "High Resolution Near-Field Electromagnetic Holography for Dynamic Source Identification in Underwater Mediums," *Progress in Electromagetic Research,* vol. 65, pp. 109-127, 2016.

[18] D. Colton and R. Kress, Inverse Acoustic and Electromagnetic Scattering Theory, Springer, 1998.

[19] H. Barucq, C. Bekkey and R. Djellouli, "Full Aperture Reconstruction of the Acoustic Far-Field Pattern from Few Measurements," *Communications on Computational Physics,* vol. 11, pp. 647-659, 2012.

[20] Z. Shen, K. Chuan Toh and S. Yun, "An Accelerated Proximal Gradient Algorithm for Nuclear Norm Regularized Linear Least Squares Problems," *Pacific Journal of Optimization*, pp. 615-640, 2010.

[21] T. Dogaru, K. Gallagher and C. Le, "Doppler Radar Phenomenology in Small Commercial Unmanned Aerial Systems," in *IEEE International Symposium on Antennas and Propagation and USNC/URSI National Radio Science Meeting*, 2017.